

High-Order Mesh Morphing for Boundary and Interface Fitting to Implicit Geometries

Jorge-Luis Barrera¹, Tzanio Kolev¹, Ketan Mittal^{1,2}, Vladimir Tomov¹

Abstract

We propose a method that morphs high-order meshes such that their boundaries and interfaces coincide/align with implicitly defined geometries. Our focus is particularly on the case when the target surface is prescribed as the zero isocontour of a smooth discrete function. Common examples of this scenario include using level set functions to represent material interfaces in multimaterial configurations, and evolving geometries in shape and topology optimization. The proposed method formulates the mesh optimization problem as a variational minimization of the sum of a chosen mesh-quality metric using the Target-Matrix Optimization Paradigm (TMOP) and a penalty term that weakly forces the selected faces of the mesh to align with the target surface. The distinct features of the method are use of a source mesh to represent the level set function with sufficient accuracy, and adaptive strategies for setting the penalization weight and selecting the faces of the mesh to be fit to the target isocontour of the level set field. We demonstrate that the proposed method is robust for generating boundary- and interface-fitted meshes for curvilinear domains using different element types in 2D and 3D.

Keywords: High-order, Implicit meshing, Mesh morphing, r -adaptivity, Finite elements, TMOP

1. Introduction

High-order finite element (FE) methods are becoming increasingly relevant in computational science and engineering disciplines due to their potential for better simulation accu-

*Performed under the auspices of the U.S. Department of Energy under Contract DE-AC52-07NA27344 and was supported by the LLNL-LDRD Program under Project No 22-ERD-023 (LLNL-JRNL-837413).

¹Lawrence Livermore National Laboratory, 7000 East Avenue, Livermore, CA 94550

²Corresponding author, mittal3@llnl.gov

racy and favorable scaling on modern architectures [1, 2, 3, 4]. A vital component of these methods is high-order computational meshes for discretizing the geometry. Such meshes are essential for achieving optimal convergence rates on domains with curved boundaries/interfaces, symmetry preservation, and alignment with the key features of the flow in moving mesh simulations [5, 6, 7].

To fully benefit from high-order geometry representation, however, one must be able to control the quality and adapt the properties of a high-order mesh. Two common requirements for mesh optimization methods are (i) to fit certain mesh faces to a given surface representation, and (ii) to perform tangential node movement along a mesh surface. This paper is concerned with these two requirements, in the particular case when the surface representation is a discrete (or implicit) function. Common examples of this scenario include use of level set functions to represent curvilinear domains as a combination of geometric primitives in Constructive Solid Geometry (CSG) [8], material interfaces in multimaterial configurations [9], and evolving geometries in shape and topology optimization [10, 11, 12], amongst other applications.

Boundary conforming high-order meshes are typically generated by starting with a conforming linear mesh that is projected to a higher order space before the mesh faces are curved to fit the boundary [13, 14, 15, 16, 17, 18, 19]. In context of boundary fitting, a closely related work is Rangarajan’s method for tetrahedral meshes [20] where an immersed linear mesh is trimmed, projected to a surface defined using a point-cloud, and smoothed to generate a high-order boundary fitted mesh. Other related approaches are Mittal’s distance function-based approach for tangential relaxation during optimization of initially fitted high-order meshes [21] and the *DistMesh* algorithm where Delaunay triangulations are aligned to implicitly defined domains using force balance. Note that we are interested in generating boundary fitted meshes using mesh morphing because it offers a way to use existing finite element framework for adapting meshes to the problem of interest. An alternative is classic mesh generation, which is usually a pre-processing step, and has been an area of interest to the meshing community for decades; summarizing different mesh generation techniques is beyond the scope of this work and the reader is referred to [22, 23, 24] for a review on this topic.

For generating interface fitted meshes, existing methods mainly rely on topological operations where the input mesh is split across the interface to generate an interface conforming mesh [25, 26]. Some exceptions are Ohtake’s method for adapting linear triangular surface meshes to align with domains with sharp features [27] and Le Goff’s method for aligning meshes to interfaces prescribed implicitly using volume fractions [28]. Barring [29, 20, 30, 27, 28], existing methods mainly rely on an initial conforming meshing for boundary fitting and on topological operations such as splitting for interface fitting.

We propose a boundary and interface fitting method for high-order meshes that is algebraic and seldom requires topological operations, extends to different element types (quadrilaterals/triangles/hexahedra/tetrahedra) in 2D and 3D, and works for implicit parameterization of the target surface using discrete finite element (FE) functions. We formulate the implicit meshing challenge as a mesh optimization problem where the objective function is the sum of a chosen mesh-quality metric using the Target-Matrix Optimization Paradigm (TMOP) [31, 32] and a penalty term that weakly forces nodes of selected faces of a mesh to align with the target surface prescribed as the zero level set of a discrete function. Additionally, we use an adaptive strategy to choose element faces/edges for alignment/fitting and set the penalization weight, to ensure robustness of the method for nontrivial curvilinear boundaries/interfaces. We also introduce the notion of a source mesh that can be used to accurately represent the level set with sufficient accuracy. This mesh is decoupled from the mesh being optimized, which allows to represent the domain of interest with higher level of detail. This approach is crucial for cases where the target boundary is beyond the domain of the mesh being optimized or the input mesh does not have sufficient resolution around the zero level set.

The remainder of the paper is organized as follows. In Section 2 we review the basic TMOP components and our framework to represent and optimize high-order meshes. The technical details of the proposed method for surface fitting and tangential relaxation are described in Section 3. Section 4 presents several academic tests that demonstrate the main features of the methods, followed by conclusions and direction for future work in Section 5.

2. Preliminaries

In this section, we describe the key notation and our prior work that is relevant for understanding our newly developed boundary- and interface-fitting method.

2.1. Discrete Mesh Representation

In our finite element based framework, the domain $\Omega \in \mathbb{R}^d$, $d = \{2, 3\}$, is discretized as a union of N_E curved mesh elements, each of order p . To obtain a discrete representation of these elements, we select a set of scalar basis functions $\{\bar{w}_i\}_{i=1}^{N_p}$, on the reference element \bar{E} . For example, for tensor-based elements (quadrilaterals in 2D, hexahedra in 3D), we have $N_p = (p + 1)^d$, and the basis spans the space of all polynomials of degree at most p in each variable, denoted by Q_p . These p th-order basis functions are typically chosen to be Lagrange interpolation polynomials at the Gauss-Lobatto nodes of the reference element. The position of an element E in the mesh \mathcal{M} is fully described by a matrix \mathbf{x}_E of size $d \times N_p$ whose columns represent the coordinates of the element *control points* (also known as *nodes* or element *degrees of freedom*). Given \mathbf{x}_E and the positions \bar{x} of the reference element \bar{E} , we introduce the map $\Phi_E : \bar{E} \rightarrow \mathbb{R}^d$ whose image is the geometry of the physical element E :

$$x(\bar{x}) = \Phi_E(\bar{x}) \equiv \sum_{i=1}^{N_p} \mathbf{x}_{E,i} \bar{w}_i(\bar{x}), \quad \bar{x} \in \bar{E}, \quad x = x(\bar{x}) \in E, \quad (1)$$

where $\mathbf{x}_{E,i}$ denotes the i -th column of \mathbf{x}_E , i.e., the i -th node of element E . Throughout the manuscript, x will denote the position function defined by (1), while bold \mathbf{x} will denote the global vector of all node coordinates.

2.2. Geometric Optimization and Simulation-Based r -adaptivity with TMOP

The input of TMOP is the user-specified transformation matrix W , from reference-space \bar{E} to target element E_t , which represents the ideal geometric properties desired for every mesh point. Note that after discretization, there will be multiple input transformation matrices W – one for every quadrature point in every mesh element. The construction of this transformation is guided by the fact that any Jacobian matrix can be written as a composition of four geometric components:

$$W = \underbrace{\zeta}_{[\text{volume}]} \underbrace{R}_{[\text{rotation}]} \underbrace{Q}_{[\text{skewness}]} \underbrace{D}_{[\text{aspect ratio}]} . \quad (2)$$

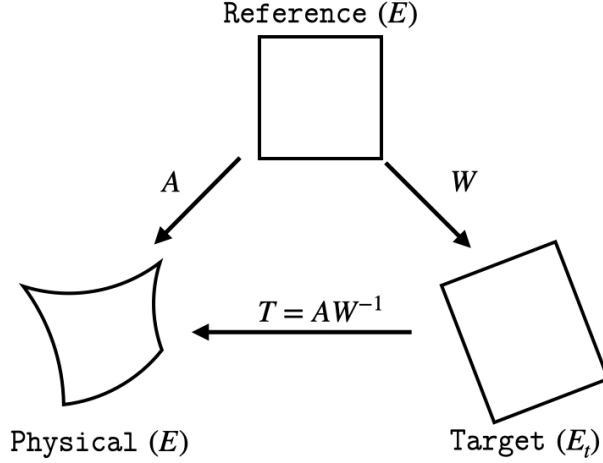


Figure 1: Schematic representation of the major TMOP matrices.

A detailed discussion on the construction of matrices associated with these geometric components and on how TMOP’s target construction methods encode geometric information into the target matrix W is given by Knupp in [33]. Various examples of target construction for different mesh adaptivity goals are given in [31, 34, 35].

Using (1), the Jacobian of the mapping Φ_E at any reference point $\bar{x} \in \bar{E}$ from the reference-space coordinates to the current physical-space coordinates is

$$A(\bar{x}) = \frac{\partial \Phi_E}{\partial \bar{x}} = \sum_{i=1}^{N_w} \mathbf{x}_{E,i} [\nabla \bar{w}_i(\bar{x})]^T. \quad (3)$$

In this manuscript, we assume that all the elements in the initial mesh are not inverted, i.e. $\det(A) > 0 \forall \bar{x} \in \bar{E}$. Combining (3) and (2), the transformation from the target coordinates to the current physical coordinates (see Fig. 1) is

$$T = AW^{-1}. \quad (4)$$

With the target transformation W defined in the domain, we next specify a mesh quality metric $\mu(T)$ that compares the transformations A and W in terms of the geometric parameters of interest. For example, $\mu_2 = \frac{|T|^2}{2\tau} - 1$ is a *shape* metric³ that depends on the skewness and aspect ratio components, but is invariant to orientation/rotation and volume. Here, $|T|$ and τ are the Frobenius norm and determinant of T , respectively. Similarly, $\mu_{77} = \frac{1}{2}(\tau - \frac{1}{\tau})^2$

³We follow the metric numbering in [36, 37].

is a *size* metric that depends only on the volume of the element. We also have *shape+size* metrics such as $\mu_{80} = \gamma\mu_2 + (1 - \gamma)\mu_{77}$ that depend on volume, skewness and aspect ratio, but are invariant to orientation/rotation. Note that the mesh quality metrics are defined such that they evaluate to 0 for an identity transformation, i.e. $\mu(T) = 0$ when $T = I$ ($A = W$). This allows us to pose the mesh optimization problem as minimization of $\mu(T)$, amongst other advantages [36].

The quality metric $\mu(T)$ is used to define the TMOP objective function for r -adaptivity

$$F(\mathbf{x}) = \sum_{E \in \mathcal{M}} F_E(\mathbf{x}_E) = \sum_{E \in \mathcal{M}} \int_{E_t} \mu(T(x)) dx_t, \quad (5)$$

where F is a sum of the TMOP objective function for each element in the mesh (F_E), and E_t is the target element corresponding to the element E . In (5), the integral is computed as

$$\sum_{E \in \mathcal{M}} \int_{E_t} \mu(T(x_t)) dx_t = \sum_{E \in \mathcal{M}} \sum_{x_q \in E_t} w_q \det(W(\bar{x}_q)) \mu(T(x_q)), \quad (6)$$

where \mathcal{M} is the current mesh with N_E elements, w_q is the quadrature weight, and the position x_q is the image of the reference quadrature point location \bar{x}_q in the target element E_t .

Optimal node locations are determined by minimizing the TMOP objective function (5). This is performed by solving $\partial F(\mathbf{x})/\partial \mathbf{x} = 0$ using the Newton's method where we improve the mesh degrees-of-freedom (nodal positions) as

$$\mathbf{x}_{k+1} = \mathbf{x}_k - \alpha \mathcal{H}^{-1}(\mathbf{x}_k) \mathcal{J}(\mathbf{x}_k). \quad (7)$$

Here, \mathbf{x}_k refers to the nodal positions at the k -th Newton iteration during r -adaptivity, α is a scalar determined by a line-search procedure, and $\mathcal{H}(\mathbf{x}_k)$ and $\mathcal{J}(\mathbf{x}_k)$ are the Hessian ($\partial^2 F(\mathbf{x}_k)/\partial \mathbf{x}_j \partial \mathbf{x}_i$) and the gradient ($\partial F(\mathbf{x}_k)/\partial \mathbf{x}_i$), respectively, associated with the TMOP objective function. The line-search procedure requires that α is chosen such that $F(\mathbf{x}_{k+1}) < 1.2F(\mathbf{x}_k)$, $|\mathcal{J}(\mathbf{x}_{k+1})| < 1.2|\mathcal{J}(\mathbf{x}_k)|$, and that the determinant of the Jacobian of the transformation at each quadrature point in the mesh is positive, $\det(A(\mathbf{x}_{k+1})) > 0$. These line-search constraints have been tuned using many numerical experiments and have demonstrated to be effective in improving mesh quality. For Newton's method, we solve the problem $\mathcal{H}(\mathbf{x}_k)\Delta \mathbf{x} = \mathcal{J}(\mathbf{x}_k)$ using a Krylov subspace method such as the Minimum Residual

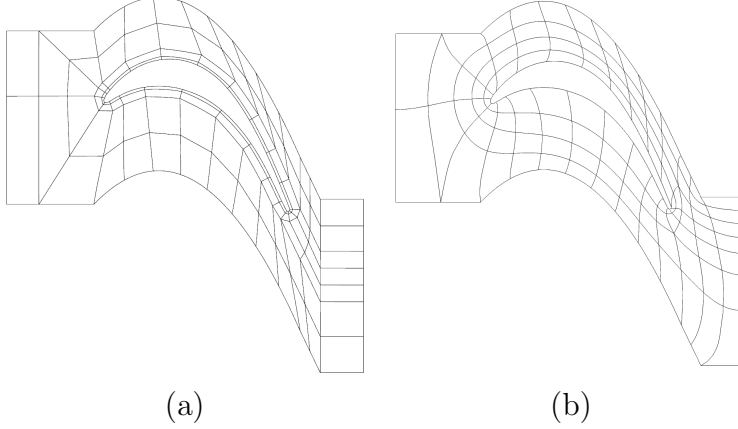


Figure 2: (a) Original and (b) optimized 4th order meshes for a turbine blade.

(MINRES) method with Jacobi preconditioning; more sophisticated preconditioning techniques can be found in [38]. Additionally, the optimization solver iterations (7) are done until the relative l_2 norm of the gradient of the objective function with respect to the current and original mesh nodal positions is below a certain tolerance ε , i.e., $|\mathcal{J}(\mathbf{x})|/|\mathcal{J}(\mathbf{x}_0)| \leq \varepsilon$. We set $\varepsilon = 10^{-10}$ for the results presented in the current work.

Using the approach described in this section, we have demonstrated r -adaptivity with TMOP for geometry and simulation-driven optimization; see Fig. 2 for example of high-order mesh optimization for a turbine blade using $W = I$ with a shape metric. The resulting optimized mesh has elements closer to unity aspect ratio and skewness closer to $\pi/2$ radians in comparison to the original mesh, as prescribed by the target $W = I$.

3. Boundary & Interface Fitting

Our goal for boundary and interface fitting is to enable alignment of a selected set of mesh nodes to some target surface of interest prescribed as the zero isocontour of a smooth signed-discrete level set function, $\sigma(x)$. Figure 3(a) and (b) show a simple example of a circular interface represented using a level set function and a triangular mesh with multimaterial interface that is to be aligned to the circular interface. To effect alignment with the zero isocontour of $\sigma(x)$, we modify the TMOP objective function (5) as:

$$F(\mathbf{x}) = \underbrace{\sum_{E \in \mathcal{M}} \int_{E_t} \mu(T(x)) dx_t}_{F_\mu} + w_\sigma \underbrace{\sum_{s \in S} \sigma^2(x_s)}_{F_\sigma}. \quad (8)$$

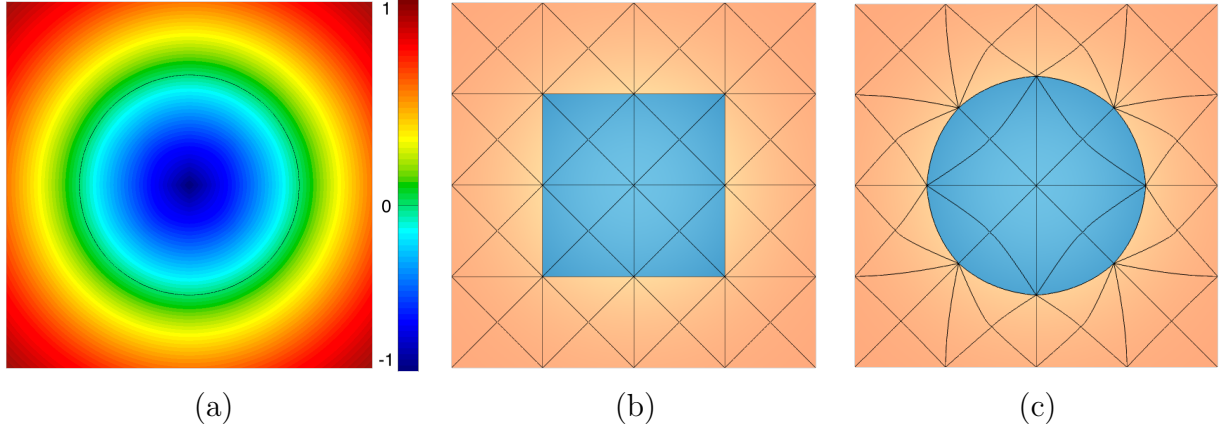


Figure 3: (a) Level set function $\sigma(x)$, (b) a Cartesian mesh with material interface nodes to be aligned to the zero level set of $\sigma(x)$, and (c) the optimized mesh.

Here, F_σ is a penalty-type term that depends on the penalization weight w_σ , the set of nodes \mathcal{S} to be aligned to the level set (e.g., the mesh nodes discretizing the material interface in Fig. 3(b)), and the level set function $\sigma(x)$, evaluated at the positions x_s of all nodes $s \in \mathcal{S}$. The F_σ term penalizes the nonzero values of $\sigma(x_s)$ for all $s \in \mathcal{S}$. Minimizing this term represents weak enforcement of $\sigma(x_s) = 0$, only for the nodes in \mathcal{S} , while ignoring the values of σ for the nodes outside \mathcal{S} . Minimizing the full nonlinear objective function, $F = F_\mu + F_\sigma$, produces a balance between mesh quality and surface fitting. Note that all nodes are treated together, i.e., the nonlinear solver makes no explicit separation between volume nodes of \mathcal{M} and the nodes $s \in \mathcal{S} \subseteq \mathcal{M}$ set for fitting. Furthermore, as there is no pre-determined unique target position for each node of \mathcal{S} , the method naturally allows tangential relaxation along the interface of interest, so that mesh quality can be improved while maintaining a good fit to the surface. Figure 3(c) shows an example of a triangular mesh fit to a circular interface using (8). In this example, we use the shape metric μ_2 with equilateral targets and a constant penalization weight, $w_\sigma = 10^3$.

The first step in our method is to use a suitable strategy for representing the level set function with sufficient accuracy (Section 3.1). Next, we determine the set of nodes \mathcal{S} that will be aligned to the zero level set of σ . For boundary fitting, \mathcal{S} depends on the elements located on the boundary of interest. For interface fitting, \mathcal{S} is the set of nodes shared between elements with different fictitious material indicators, and we describe our approach for setting the material indicators of elements in Section 3.2. Finally, we set the penalization

weight w_σ such that an adequate fit is achieved to the target surface while optimizing the mesh with respect to the quality metric μ (Section 3.3). The adaptive strategy for setting w_σ requires us to modify the line-search and convergence criterion of the Newton’s method (Section 3.4). For completeness, the derivatives of F_σ are discussed in Section 3.5. Using various examples, we demonstrate in Section 4 that our method extends to both simplices and hexahedrals/quadrilaterals of any order, and is robust in adapting a mesh interface and/or boundary to nontrivial curvilinear shapes.

3.1. Level Set Representation

The following discussion is related to the case when $\sigma(x)$ is a discrete function so that its values and derivatives can’t be computed analytically. Then the first step in our implicit meshing framework is to ensure that the level set function $\sigma(x)$ is defined with sufficient accuracy. A drawback of discretizing $\sigma(x)$ on the mesh being optimized, \mathcal{M} , is that the resulting mesh will be sub-optimal in terms of mesh quality and interface/boundary fit if (a) the mesh does not have enough resolution to represent $\sigma(x)$ with sufficient accuracy, especially near the zero level set, or (b) the target level set is outside the initial domain of the mesh. For the latter, it’s impossible to compute the necessary values and derivatives of the level set function accurately at the boundary nodes that we wish to fit, once the mesh moves outside the initial domain; see Figure 4(a) for an example.

To address these issues, we introduce the notion of a background/source mesh (\mathcal{M}_B) for discretizing $\sigma(x_B)$, where x_B represents the positions of the source mesh nodes, as in

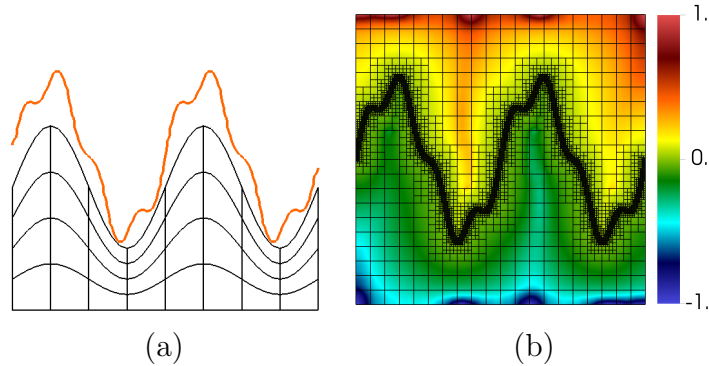


Figure 4: Using a background mesh to fit discretely prescribed domain boundaries. (a) Initial unfitted mesh and target boundary curve (orange). (b) The boundary curve is prescribed implicitly as the zero level set of a discrete function on an adaptively refined nonconforming background mesh.

(1). Since \mathcal{M}_B is independent of \mathcal{M} , we can choose \mathcal{M}_B based on the desired accuracy; the maximum error in representing the implicit geometry discretely is bounded by the element size of the background mesh at the location of the zero level set. Thus, we use adaptive nonconforming mesh refinements [39] around the zero level set of $\sigma(x_B)$, as shown in Fig. 4(b). Using a source mesh for $\sigma(x_B)$, however, requires transfer of the level set function and its derivatives from \mathcal{M}_B to the nodes $\mathcal{S} \in \mathcal{M}$ prior to each Newton iteration. This transfer between the source mesh and the current mesh is done using *gslib*, a high-order interpolation library [40]:

$$\sigma(x) = \mathcal{I}(x, x_B, \sigma(x_B)), \quad \partial\sigma(x) = \mathcal{I}(x, x_B, \partial\sigma(x_B)), \quad \partial^2\sigma(x) = \mathcal{I}(x, x_B, \partial^2\sigma(x_B)), \quad (9)$$

where \mathcal{I} represent the interpolation operator that depends on the current mesh nodes (x), the source mesh nodes (x_B), and the source function $\sigma(x_B)$ or its gradients. A detailed description of how high-order functions can be transferred from a mesh to an arbitrary set of points in physical space using *gslib* is described in Section 2.3 of [41].

While surfaces such as the circular interface in Fig. 3 and sinusoidal boundary in Fig. 4 are straightforward to define using smooth level-set functions, more intricate domains are typically defined as a combination of non-smooth functions for different geometric primitives, which are not well suited for our penalization-based formulation (8). Consider for example a two-material application problem in Fig. 5(a) where the domain is prescribed as a combina-

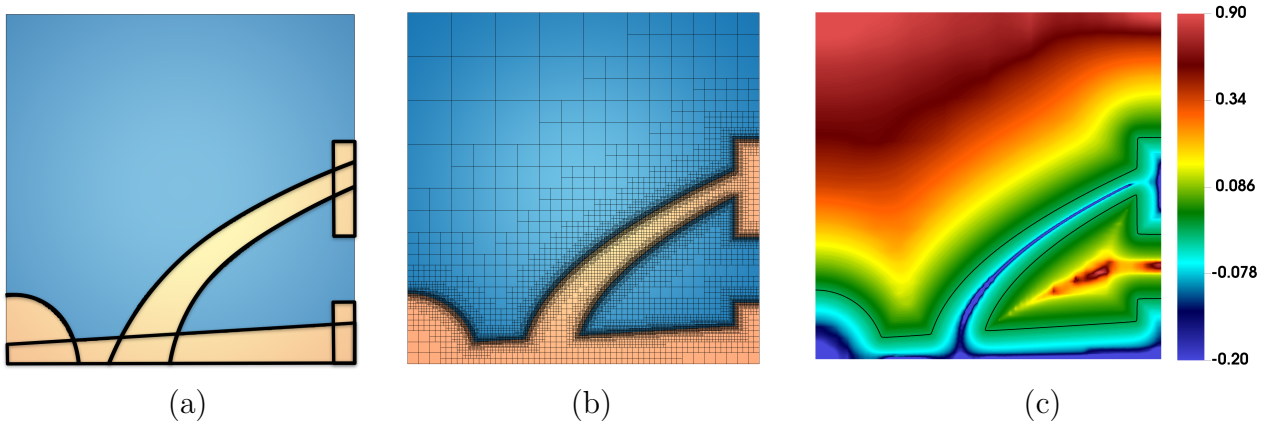


Figure 5: Multimaterial domain for a target application. (a) Domain modeled using geometric primitives with $\mathcal{G}(\mathbf{x}_B) = 1$ (orange) and -1 (blue), (b) background mesh with adaptive mesh refinements around the zero level set of $\mathcal{G}(\mathbf{x}_B)$, and (c) distance function calculated on the background mesh [42] to be used as $\sigma(x)$ in (8).

tion of geometric primitives for a circle, rectangle, parabola, and a trapezium. The resulting step function $\mathcal{G}(x_B)$ is 1 inside one material and -1 inside the other material. For such cases, we start with a coarse background mesh and use adaptive mesh refinement around the zero level set of $\mathcal{G}(x_B)$, see Fig 5(b). Then we compute a discrete distance function using the p-Laplacian solver of [42], Section 7, from the zero level set of $\mathcal{G}(x_B)$, see Fig 5(c). The advantage of using this distance function in (8) is that it is (i) generally smoother and (ii) maintains the location of the zero level set.

3.2. Setting \mathcal{S} for Interface Fitting

For interface fitting, the set \mathcal{S} contains the nodes that are used to discretize the material interface in the mesh. As demonstrated in this section, the accuracy of the fitting to the target surface using (8) depends on the combination of the (i) mesh topology around the interface, and (ii) the shape of the target surface. Thus, for a given initial mesh and implicit interface, it is important to choose the fictitious material indicator of elements such that the resulting material interface is compatible with the target surface.

Consider for example the triangular mesh shown in Figure 6(a) which must be aligned to a circular level set. A naive approach for setting the material indicators is to partition the mesh into two fictitious materials based on the level-set function sampled at the set \mathcal{Q} of quadrature points inside each element. For example, the material indicator η_E for element E can be set using the integral of $\sigma(x)$ as:

$$\eta_E = \begin{cases} 0, & \text{if } \int_E \sigma(x) \geq 0 \\ 1, & \text{otherwise} \end{cases}, \quad (10)$$

or using the maximum norm of $\sigma(x)$ as:

$$\eta_E = \begin{cases} 0, & \text{if } \max_{q \in \mathcal{Q}} |\sigma(x_q)| \geq 0 \\ 1, & \text{otherwise.} \end{cases}. \quad (11)$$

Using such approaches can lead to elements that have multiple adjacent faces as a part of the material interface of the mesh (highlighted in red). When the mesh deforms for fitting, this results in sub-optimal Jacobians in the elements at the vertex shared by the (highlighted) adjacent faces. This is evident in Figure 6(b) where the material indicator is set using (10).

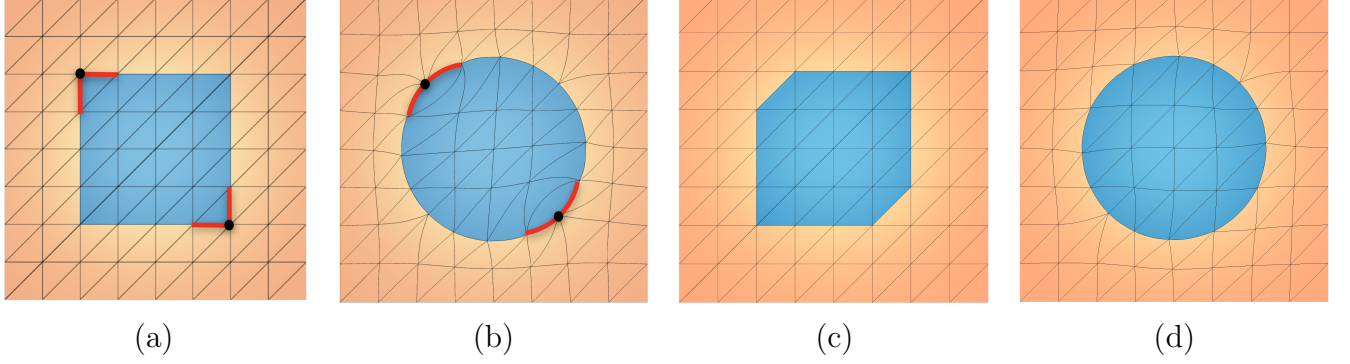


Figure 6: (a) Triangular mesh with material indicators of elements using (10) and the (b) optimized mesh. (c) Mesh with material indicators of elements using (12) and the resulting (d) optimized mesh.

The fundamental issue here is that whenever adjacent faces of an element are aligned to a level set, the resulting mesh quality and fit can be sub-optimal depending on the complexity of the target shape/geometry. To address this issue, we update the material indicator for each element in the mesh as:

$$\tilde{\eta}_E = \begin{cases} \eta_E, & \text{if } N_{E,M} \leq 1 \\ 1 - \eta_E, & \text{else if } N_{E,M} = N_{E,F} - 1, \\ \eta_E, (\text{optionally}) \text{ mark } E \text{ for splitting} & \text{otherwise} \end{cases} \quad (12)$$

where $N_{E,M}$ is the number of faces of element E that are part of the material interface, and $N_{E,F}$ is the total number of faces of element E . Note that (12) is formulated as a two pass approach where we first loop over all elements with $\eta_E = 0$ and then with $\eta_E = 1$. This approach ensures that conflicting decisions are not made for adjacent elements surrounding the interface.

The first condition in (12) keeps the original material indicator of an element when one of its faces is to be aligned to the level set. The second condition switches the material indicator of an element if all but one of the faces of an element is to be aligned, thus resulting in only one of its faces to be aligned after the switch. These two conditions are usually sufficient to guarantee that at most one face per element is set for alignment in triangular meshes. Figures 6(c, d) show an example of material interface that results from (12), which avoids the issue of sub-optimal Jacobian at the vertex shared by adjacent faces.

In quadrilateral elements, when $1 < N_{E,M} < N_{E,F} - 1$ (i.e. $N_{E,M} = 2$), we can optionally

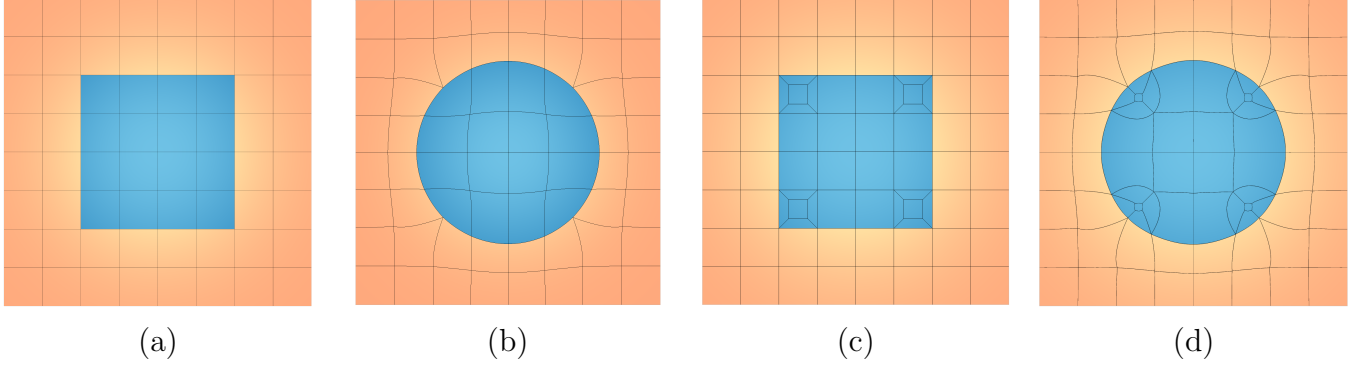


Figure 7: (a) Quadrilateral mesh with material indicators using the strategy in (10) and the (b) optimized mesh. (c) Mesh material indicators set using (12) with conforming split introduced for elements with 2 faces marked for fitting, and (d) the resulting optimized mesh.

do conforming splits on each element to bisect the vertex connecting adjacent faces that have been marked for fitting. This approach results in elements that have only 1 face marked for alignment, as long as the elements resulting from split keep the material indicator of the original element. Conforming mesh refinements increase the computational cost due to increased number of degrees-of-freedom, but lead to a better mesh quality. Figure 7 shows an example of a comparison of a quadrilateral mesh fit to the circular level set using (10) and (12).

Note that conforming splits can also be done for triangles, if needed, by connecting each of its vertex to the centroid of the triangle. For tetrahedra and hexahedra, conforming splits independent of adjacent elements are not yet possible, and we are currently exploring nonconforming refinement strategies. Nonetheless, if such a situation arises where multiple adjacent faces of an element are marked for fitting, the proposed method will still align the mesh the best it can under the constraint of a prescribed threshold on minimum Jacobian in the mesh (15).

3.3. Adaptive Penalization Weight

Recall that the balance between mesh quality and node fitting is controlled by the penalization weight w_σ in (8). Numerical experiments show that use of a constant w_σ requires tweaking on a case-by-case basis, and can result in a sub-optimal fit if w_σ is too small, in which case the objective function is dominated by the mesh quality metric term, or if w_σ is too large, in which case the conditioning of the Hessian matrix is poor. Figure 8 demon-

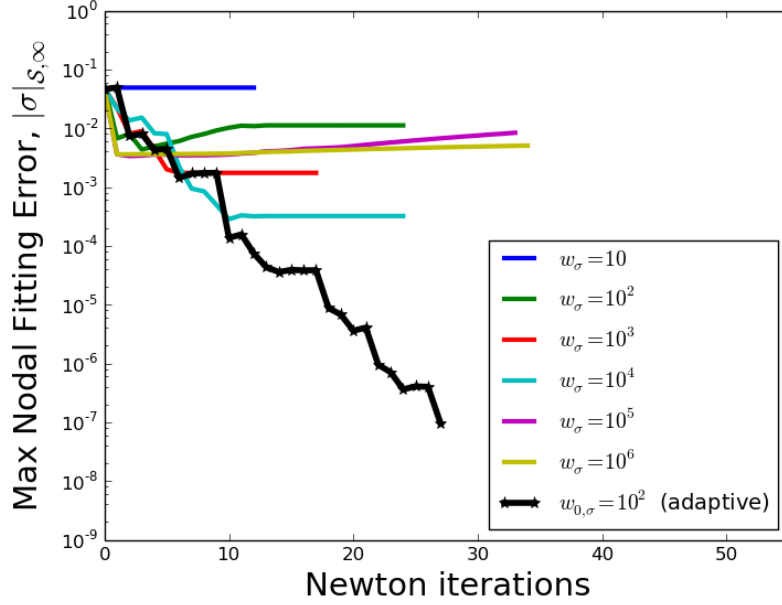


Figure 8: Impact of w_σ on the surface fitting error.

strates how the maximum surface fitting error varies for a uniform quad mesh fit to a circular interface (recall Figure 7(a, b)) for different fixed values of w_σ . Here, we define the maximum surface fitting error as the maximum value of the level set function evaluated at the nodes $s \in \mathcal{S}$:

$$|\sigma|_{\mathcal{S}, \infty} := \max_{s \in \mathcal{S}} |\sigma(x_s)|.$$

Figure 8 shows that as we increase w_σ from 1 to 10^4 , the fitting error decreases. However, the error worsens if we increase w_σ further.

To address this issue we use an adaptive approach for setting w_σ where we monitor $|\sigma|_{\mathcal{S}, \infty}$, and scale w_σ by a user-defined constant ($\alpha_\sigma = 10$ by default) if the relative decrease in the maximum nodal fitting error between subsequent Newton iterations is below a prescribed threshold ($\epsilon_{\Delta\sigma} = 0.001$ by default). That is,

$$w_{k+1, \sigma} = \begin{cases} \alpha_\sigma \cdot w_{k, \sigma} & \text{if } \frac{|\sigma|_{k, \mathcal{S}, \infty} - |\sigma|_{k+1, \mathcal{S}, \infty}}{|\sigma|_{k+1, \mathcal{S}, \infty}} < \epsilon_{\Delta\sigma} \\ w_{k, \sigma} & \text{otherwise} \end{cases}, \quad (13)$$

where we use the subscript k to denote a quantity at the k th Newton iteration. Figure 8 shows that this adaptive approach for setting w_σ significantly improves the quality of the mesh fit to the desired level set. Updating the value of w_σ changes the definition of the

objective function (8), which requires some modifications of the line search and convergence criterion of the Newton iterations to achieve overall convergence, compared to the constant w_σ case; details will follow in Section 3.4. Nevertheless, our numerical tests suggest that this impact is negligent in comparison to the improvement of the fitting error.

3.4. Convergence & Line-Search Criterion

Recall that in the general TMOP approach, the line-search and convergence criteria for the Newton's method are based on the magnitude and the derivatives of the objective function, see Section 2.2. In the penalization-based formulation (8), the current criteria do not suffice because the magnitude and derivatives of the objective function depend on the penalization weight $w_{k,\sigma}$, which can change between subsequent Newton iterations due to (13).

We modify our line-search criteria by adding two additional inequalities, namely, α in (7) is chosen to ensure:

$$|\sigma|_{k+1,\mathcal{S},\infty} < 1.2 |\sigma|_{k,\mathcal{S},\infty}, \quad (14)$$

$$\min(\det(A(\mathbf{x}_{k+1}))) > 0.001 \cdot \min(\det(A(\mathbf{x}_0))). \quad (15)$$

The inequality (14) prevents sudden jumps of the fitting error, and the scaling factor 1.2 has been chosen empirically. The constraint (15) is mostly applicable in regimes when w_σ is big enough to make the quality term F_μ effectively inactive. Such regimes represent a situation when one is willing to sacrifice mesh quality for more accurate fitting. When the quality term F_μ is relatively small, it may be unable to prevent the appearance of infinitesimally small positive Jacobians; the constraint (15) is used to alleviate this situation.

The convergence criterion is also modified to utilize the fitting error, i.e., the Newton's method is used until $|\sigma|_{\mathcal{S},\infty}$ is below a certain user-specified threshold ($\epsilon_\sigma = 10^{-5}$ by default). We also use an optional convergence criterion based on a limit on the maximum number of consecutive Newton iterations through which the penalization weight w_σ is adapted using (13); this limit is $N_\sigma = 10$ by default. This latter criterion avoids excessive computations in cases where the mesh topology does not allow the fitting error to reduce beyond a certain limit.

3.5. Derivatives

As our default choice for nonlinear optimization is the Newton's method, we must compute first and second order derivatives of F_μ and F_σ with respect to the mesh nodes. The definition of the derivatives of F_μ is given in Sections 3.3 and 3.4 of [43], and here we focus on the derivatives of F_σ . Let the FE position function be $x = (x_1 \dots x_d)^T$ where d is the space dimension; each component can be written as $x_a(\bar{x}) = \sum_i x_{a,i} \bar{w}_i(\bar{x})$, where $x = x(\bar{x})$, see Section 2.1. Then the Newton's method solves for the full vector

$$\mathbf{x} = (x_{1,1} \dots x_{1,N_x}, x_{2,1} \dots x_{2,N_x} \dots x_{d,N_x})^T$$

that contains the positions of all mesh nodes. The formulas for the first and second derivatives of F_σ are the following:

$$\begin{aligned} \frac{\partial F_\sigma(\mathbf{x})}{\partial x_{a,i}} &= 2\omega_\sigma \sum_{s \in \mathcal{S}} \sigma(x_s) \frac{\partial \sigma(x_s)}{\partial x_a} \frac{\partial x_a(\bar{x}_s)}{\partial x_{a,i}} = 2\omega_\sigma \sum_{s \in \mathcal{S}} \sigma(x_s) \frac{\partial \sigma(x_s)}{\partial x_a} \bar{w}_i(\bar{x}_s), \\ \frac{\partial^2 F_\sigma(\mathbf{x})}{\partial x_{b,j} \partial x_{a,i}} &= 2\omega_\sigma \sum_{s \in \mathcal{S}} \left(\frac{\partial \sigma(x_s)}{\partial x_b} \frac{\partial \sigma(x_s)}{\partial x_a} + 2\omega_\sigma \frac{\partial^2 \sigma(x_s)}{\partial x_b \partial x_a} \right) \bar{w}_i(\bar{x}_s) \bar{w}_j(\bar{x}_s), \\ a, b &= 1 \dots d, \quad i, j = 1 \dots N_x. \end{aligned} \tag{16}$$

The above formulas require the spatial gradients of σ at the current positions $\{x_s\}_{s \in \mathcal{S}}$ of the marked nodes. These gradients can be closed-form expressions, when σ is prescribed analytically, or the gradients are obtained from the background mesh \mathcal{M}_B (see Section 3.1), when σ is a discrete function.

3.6. Algorithm/Summary

In this section, we summarize our penalization-based method for boundary and interface fitting with TMOP. The inputs to our method are the active/current mesh \mathcal{M} that is defined through the global vector \mathbf{x} of nodal positions, a user-selected target construction option to form W as in (2), a mesh quality metric μ , a source/background mesh with nodal coordinates \mathbf{x}_B along with the level set function $\sigma(x_B)$ as explained in Section 3.1, initial penalization weight w_σ , parameters for adaptive penalization-weight (α_σ and $\epsilon_{\Delta\sigma}$ as in Section 3.3), and parameters for convergence criterion ϵ_σ and N_σ as in Section 3.4. Algorithm 1 summarizes our penalization-based method where we use subscript $k = 0 \dots N_{opt}$ to denote different quantities at the k th Newton iteration.

Algorithm 1: Implicit Meshing

Input: \mathbf{x} , μ , \mathbf{x}_B , $\sigma(x_B)$, α_σ , $\epsilon_{\Delta\sigma}$, w_σ , ϵ_σ , N_{opt} **Output:** \mathbf{x}_s

```
1  $n_\sigma := 0$ ,  $k = 0$ ,  $\mathbf{x}_0 = \mathbf{x}$ 
2 Determine  $\mathcal{S}$ , the set of nodes for fitting (Section 3.2)
3  $\sigma(\mathbf{x}_0) = \mathcal{I}(\mathbf{x}_0, \mathbf{x}_B, \sigma(\mathbf{x}_B))$ 
4 while  $|\sigma|_{k,\mathcal{S},\infty} > \epsilon_\sigma$  and  $n_\sigma < N_\sigma$  and  $k < N_{opt}$  do
5    $W_i = I$  for each quadrature point  $i$  [33].
6    $\mathcal{H}(\mathbf{x}_k)\Delta\mathbf{x} = \mathcal{J}(\mathbf{x}_k) \rightarrow$  solve using MINRES (Section 2.2).
7    $\mathbf{x}_{k+1} = \mathbf{x}_k - \alpha\Delta\mathbf{x}$ , with  $\alpha$  determined using line-search (Section 3.4).
8   if  $\frac{|\sigma|_{k,\mathcal{S},\infty} - |\sigma|_{k+1,\mathcal{S},\infty}}{|\sigma|_{k+1,\mathcal{S},\infty}} < \epsilon_{\Delta\sigma}$  then
9      $w_{k+1,\sigma} \rightarrow \alpha_\sigma \cdot w_{k,\sigma}$ 
10     $n_\sigma = 0$ 
11  else
12     $n_\sigma = n_\sigma + 1$ 
13  end
14   $\sigma(\mathbf{x}_{k+1}) = \mathcal{I}(\mathbf{x}_{k+1}, \mathbf{x}_B, \sigma(\mathbf{x}_B))$ 
15   $k = k + 1$ 
16 end
17  $\mathbf{x} = \mathbf{x}_k$ 
```

4. Numerical Results

In this section, we demonstrate the main properties of the method using several examples. The presented tests use $W = I$ as the target matrix, and the following shape metrics:

$$\begin{aligned} \mu_2 &= \frac{|T|^2}{2\tau} - 1, \\ \mu_{303} &= \frac{|T|^2}{3\tau^{2/3}} - 1, \end{aligned} \tag{17}$$

where $|T|$ and τ are the Frobenius norm and determinant of T , respectively. Both metrics are polyconvex in the sense of [44, 45], i.e., the metric integral F_μ in (5) theoretically has a

minimizer. Exploring the effect of the smoothness of $\sigma(x)$ on the convexity of the objective function (8) will be the subject of future studies.

Our implementation utilizes MFEM, a finite element library that supports arbitrarily high-order spaces and meshes [3]. This implementation is freely available at <https://mfem.org>.

4.1. Fitting to a Spherical Interface

As a proof of concept, we adapt 3rd order hexahedral (hex) and tetrahedral (tet) meshes to align to a spherical surface; see Figure 9(a) and (b). The domain is a unit-sized cube, $\Omega \in [0, 1]^3$, and the level set function σ representing the sphere is defined such that its zero isosurface is located at a distance of 0.3 from the center of the domain ($x_c = (0.5, 0.5, 0.5)$). Although this level set is simple enough to be defined analytically, the presented computations represent and use σ as a discrete finite element function. Additionally, no background mesh is used in this example, i.e., $\mathbf{x}_B = \mathbf{x}$.

The initial hex mesh is an $8 \times 8 \times 8$ Cartesian-aligned mesh. The material indicators are setup such that there are a total of 32 elements that have more than one face marked for fitting. The tet mesh is obtained by taking a 4×4 Cartesian-aligned hex mesh and splitting each hex into 24 tetrahedra sharing a vertex at the center of the cube (4 tets-per-hex face). The material indicators are setup such that all faces marked for fitting belong to different elements. The optimized meshes, shown in Fig. 9(c) and (d), have a maximum error of $O(10^{-10})$ at the interface with respect to the zero level set, which is achieved in 76 and 44 Newton iterations for the hexahedral and tetrahedral mesh, respectively. In the

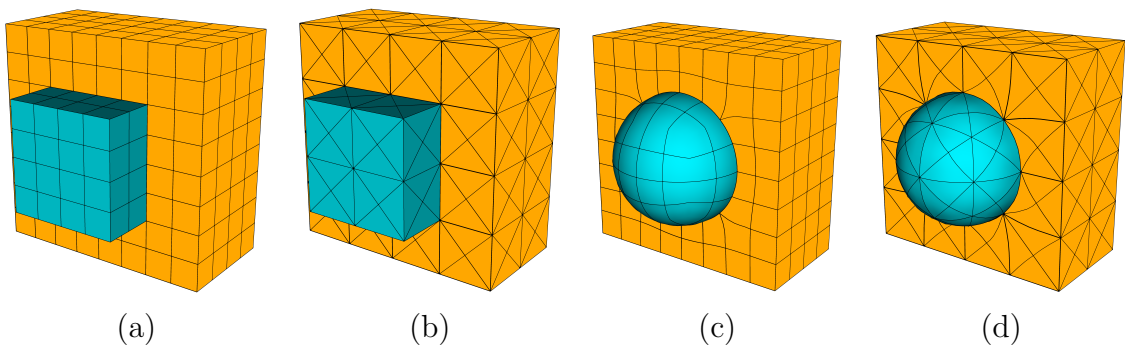


Figure 9: Initial (a) hexahedral and (b) tetrahedral meshes showing the interfaces for the 3D surface fitting tests. Optimized (c) hexahedral and (d) tetrahedral mesh obtained using (8).

tetrahedral mesh, the minimum Jacobian decreases from 4×10^{-3} to 4.6×10^{-6} and in the hexahedral mesh, the minimum Jacobian decreases from 1.2×10^{-3} to 1.5×10^{-5} during mesh optimization as the mesh deforms to align to the target surface; in both cases the minimum Jacobian appears near the fitted faces. The decrease in the Jacobian at the interface is expected, with a lower bound on the Jacobian imposed by (15) to ensure that the mesh stays valid for desired finite element computations. Note that the hexahedral mesh requires more iterations as compared to the tetrahedral mesh partly because there are multiple elements with adjacent faces marked for fitting, which requires more work from the adaptive weight mechanism to force those mesh faces to align with the spherical interface.

4.2. Boundary and Interface Fitting for Geometric Primitive-Based Domains in 3D

This example demonstrates that the proposed fitting method can be applied not only to internal interfaces, but also to high-order boundaries. The target domain is represented as a combination of simple geometric primitives, namely, an intersection of a cube ($side=0.5$, centered around $x_c = (0.5, 0.5, 0.5)$) with a sphere ($radius=0.3$, centered around x_c) that has three Cartesian-aligned cylinders ($radius=0.15$, $length=0.5$) removed from it. Figure 10 shows the CSG tree with geometric primitives and the Boolean operations that are used to construct the target geometry.

Using the approach outlined in Section 3.1, we combine the geometric primitives on a third-order source mesh that is adaptively refined five times around the zero level set of

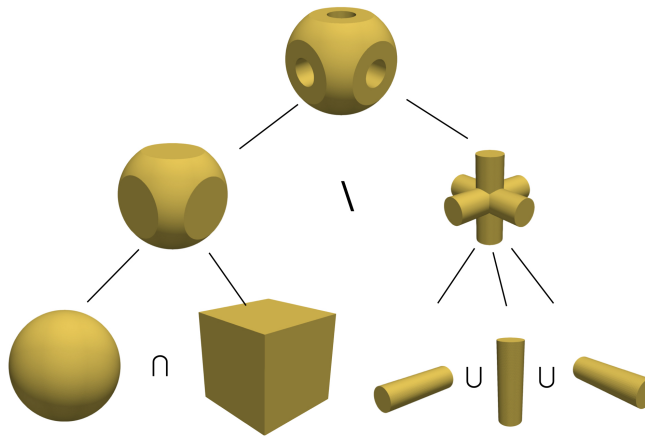


Figure 10: CSG tree with geometric primitives used to define the target geometry. Here, \cap denotes the geometric intersection operator, \cup denotes the union operation, and \setminus denotes the exclusion operator.

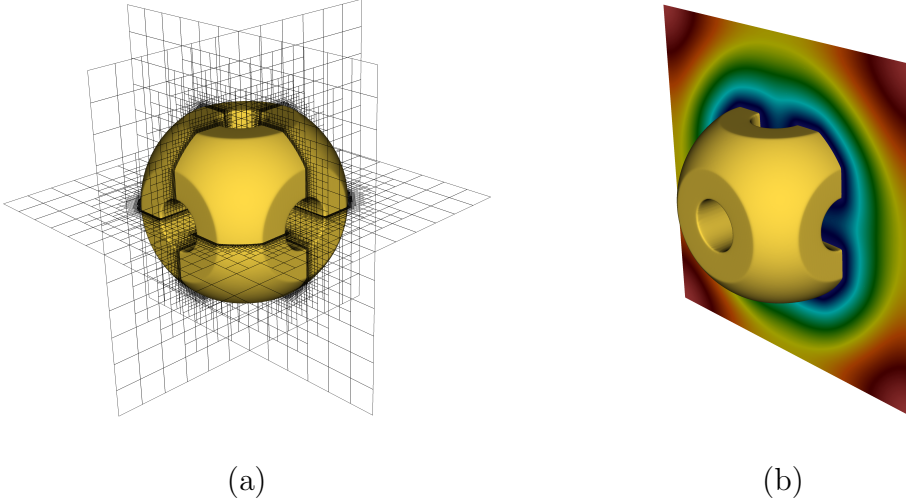
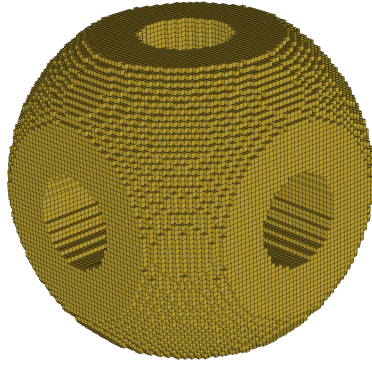


Figure 11: (a) Adaptively refined background mesh used to model the target domain, and (b) level set function computed using the distance from the zero level set of the geometric primitive-based geometry.

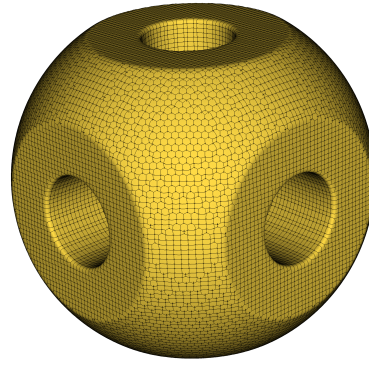
the target domain. We then compute the distance function on this background mesh using the p -Laplacian solver [42]. This distance function is used as the level set function in (8). Figure 11(a) shows a slice-view of the background mesh along with the zero iso-surface of the level set function, and Fig. 11(b) shows a slice-view of the level set function computed as the distance from the zero level set of the geometric primitive-based description of the domain. Our numerical experiments showed that using a third order source mesh with five adaptive refinements was computationally cheaper than using a lower order mesh with more adaptive refinements to obtain the same level of accuracy for capturing the the curvilinear boundary using the distance function.

The input mesh to be fit for this problem is a uniform second-order $128 \times 128 \times 128$ Cartesian-aligned mesh for $\Omega \in [0, 1]^3$. This mesh is trimmed by using (10) and removing all elements with $\eta_E = 0$. The minimum Jacobian in the trimmed mesh is 4.8×10^{-7} . The trimmed mesh is optimized using (8) where the nodes on the boundary are set for alignment. Figure 12 shows the input and the optimized mesh, where the achieved fitting error is $|\sigma|_{\mathcal{S}, \infty} = \mathcal{O}(10^{-6})$ with the minimum Jacobian at the boundary decreasing to 4.8×10^{-10} .

Other 3D applications of interest that are currently leveraging the proposed method are shown next. Figure 13(a) shows an example of one of the boundary-fitted meshes obtained for simulation and design of lattice structures in the context of additive manufacturing.



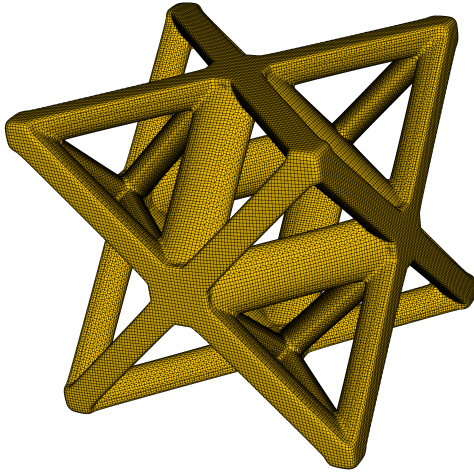
(a)



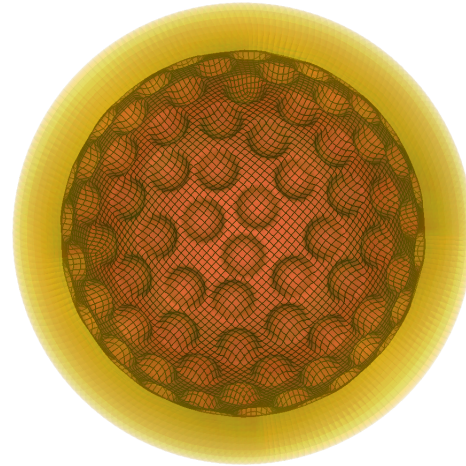
(b)

Figure 12: (a) Initial trimmed mesh and (b) final fitted mesh for the primitive-based geometry test.

Figure 13(b) shows an example of one of the interface-fitted meshes obtained for analyzing the impact of fluid flow on parameterized surfaces. Here, the target multimaterial domain consists of two concentric shells with parameterized locations and sizes for indents at the material interface. Note, the example shown in Fig. 13(b) consists of uniformly spaced indents of the same size. The inner shell is colored red and the outer shell is translucent and



(a)



(b)

Figure 13: (a) Boundary-fitted mesh generated using a geometric-primitive based description for an Octet truss. (b) Interface-fitted mesh for a multimaterial domain with concentric spherical shells with uniformly spaced indents of same size at the material interface. The inner shell is colored red and the outer shell is translucent and colored golden.

colored golden, with the mesh morphed to align to the indents highlighted at the interface.

4.3. Interface Fitting for Shape Optimization Application

This example serves to demonstrate the applicability of the proposed approach to setup the initial multimaterial domain to be used in a shape optimization problem. Figure 14 shows the cross section of a tubular reactor that consists of a highly conductive metal (*red*) and a low conductivity heat generating region (*blue*). The design optimization problem is formulated such that the energy production in the system is maximized while keeping the overall volume of the red region constant. To achieve this, the shape of the *red* subdomain is morphed using a gradient-based approach in our in-house design optimization framework that requires an interface fitted mesh as an input. This initial fitted mesh is generated using the method described in this manuscript.

Exploiting the cyclic symmetry, we discretize a portion of the domain via a triangular mesh. Since this initial mesh does not need to align with the material interface, it can be conveniently generated using an automatic mesh generator [46]. We then use an approach similar to the previous section for interface fitting where the multimaterial domain is realized as a combination of geometric primitives (annulus, parabola, and trapezium, as highlighted in Figure 14). The finite element distance function from the interface is computed using the p-Laplacian solver of [42], Section 7, and used as the level-set function $\sigma(x)$ in (8).

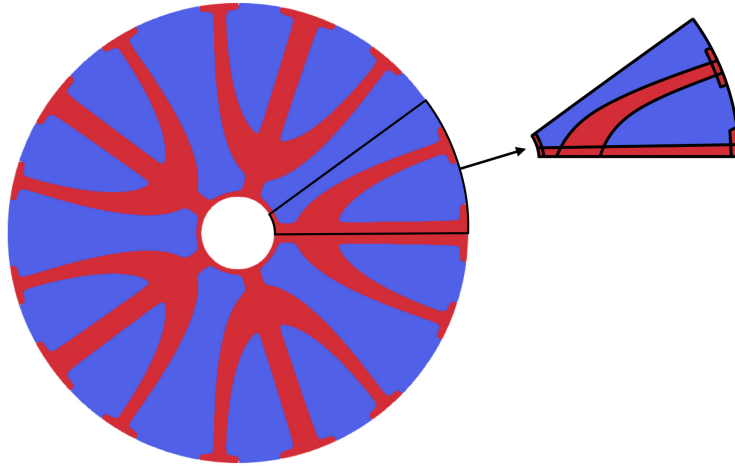


Figure 14: Reactor domain to be meshed for shape optimization, along with the symmetric portion and its primitive decomposition. The internal material interfaces must be fitted in the final mesh.

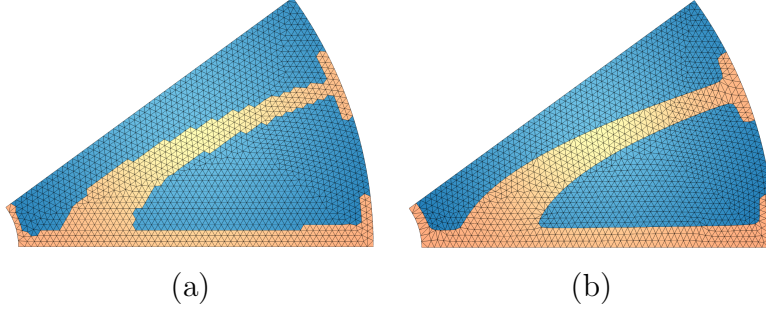


Figure 15: (a) Original mesh and (b) interface fitted mesh for the reactor design problem.

Figure 15(a) shows the input non-fitted mesh, colored by the adaptively assigned material indicator, such that there is at most one face per triangle marked for fitting. Figure 15(b) shows the adapted mesh which aligns with the material interface of the domain. The maximum interface fitting error of the optimized mesh is $\mathcal{O}(10^{-10})$, and the minimum Jacobian in the mesh decreases from 10^{-7} to 2×10^{-8} at the nodes along the interface due to mesh deformation enforcing alignment to the target surface. Finally, Figures 16(a)-(d) show the initial interface-fitted domain and the shape optimized domain along with the corresponding temperature (Kelvin) fields. As we can see, the proposed method is effective for generating high quality interface fitted meshes with minimal user intervention, and is currently being used for similar 3D shape optimization applications that will be presented in future work.

5. Conclusion & Future Work

We have presented a novel method to morph and align high-order meshes to the domain of interest. We formulate the mesh optimization problem as a variational minimization of the sum of a chosen mesh-quality metric and a penalty term that weakly forces the selected faces of the mesh to align with the target surface. The penalty-based formulation makes the proposed method suitable for adoption in existing mesh optimization frameworks.

There are three key features of the proposed method that enable its robustness. First, a source mesh is used to represent the level set function with sufficient accuracy when the mesh being morphed does not have enough resolution or is beyond the target surface (Section 3.1). Second, an adaptive approach is proposed for setting the fictitious material indicators in the mesh to ensure that the resulting material interface can align to the target surface for interface fitting (Section 3.2). Finally, an adaptive approach for setting the penalization

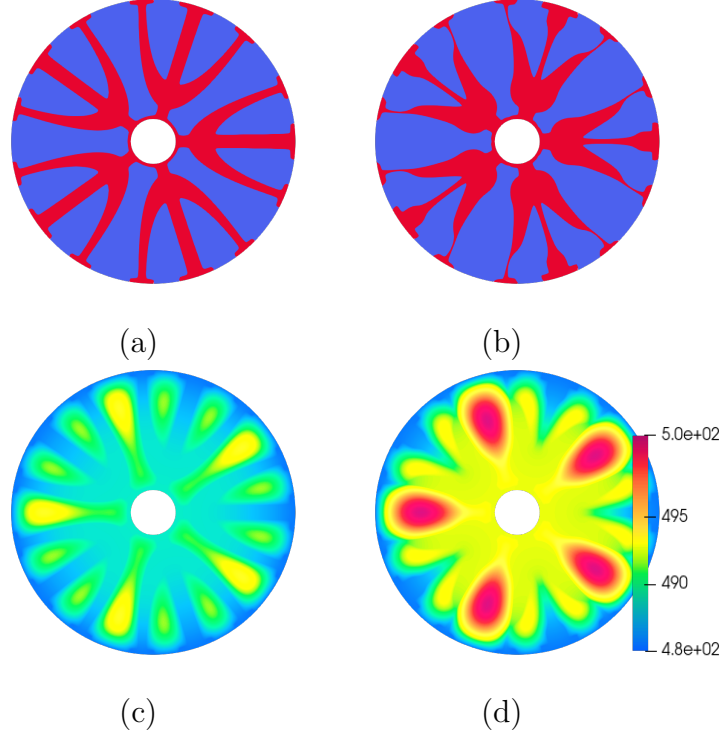


Figure 16: (a) Initial fitted domain obtained using the proposed method and (b) shape optimized domain from our in-house design optimization framework. Corresponding temperature (Kelvin) for the (c) initial domain and (d) shape optimized domain.

weight is developed to eliminate the need for tuning the penalization weight on a case-by-case basis (Section 3.3). Numerical experiments demonstrate that the proposed method is effective for generating boundary- and interface-fitted meshes for nontrivial curvilinear geometries.

In future work, we will improve the method by developing mesh refinement strategies for hexahedral and tetrahedral meshes, which are required when the mesh topology limits the fit of a mesh to the target surface (Section 3.2). We will also explore ways for aligning meshes to domains with sharp features [27, 47], as we currently assume that the level set function σ used in (8) is sufficiently smooth around its zero level set. Finally, we will also look to optimize our method and leverage accelerator-based architectures by utilizing partial assembly and matrix-free finite element calculations [43].

References

- [1] M. Deville, P. Fischer, E. Mund, High-order methods for incompressible fluid flow, Cambridge University Press, 2002. 2
- [2] P. Fischer, M. Min, T. Rathnayake, S. Dutta, T. Kolev, V. Dobrev, J.-S. Camier, M. Kronbichler, T. Warburton, K. Świrydowicz, et al., Scalability of high-performance PDE solvers, *The International Journal of High Performance Computing Applications* 34 (5) (2020) 562–586. 2
- [3] R. Anderson, J. Andrej, A. Barker, J. Bramwell, J.-S. Camier, J. Cervený, V. A. Dobrev, Y. Dudouit, A. Fisher, T. V. Kolev, W. Pazner, M. Stowell, V. Z. Tomov, I. Akkerman, J. Dahm, D. Medina, S. Zampini, MFEM: a modular finite elements methods library, *Computers & Mathematics with Applications* 81 (2020) 42–74. doi:10.1016/j.camwa.2020.06.009. 2, 18
- [4] T. Kolev, P. Fischer, M. Min, J. Dongarra, J. Brown, V. Dobrev, T. Warburton, S. Tomov, M. S. Shephard, A. Abdelfattah, V. Barra, N. Beams, J.-S. Camier, N. Chalmers, Y. Dudouit, A. Karakus, I. Karlin, S. Kerkemeier, Y.-H. Lan, D. Medina, E. Merzari, A. Obabko, W. Pazner, T. Rathnayake, C. W. Smith, L. Spies, K. Swirydowicz, J. Thompson, A. Tomboulides, V. Tomov, Efficient exascale discretizations: High-order finite element methods, *International Journal of High Performance Computing Applications* To appear (2021). 2
- [5] X.-J. Luo, M. Shephard, L.-Q. Lee, L. Ge, C. Ng, Moving curved mesh adaptation for higher-order finite element simulations, *Engineering with Computers* 27 (1) (2011) 41–50. 2
- [6] V. Dobrev, T. Kolev, R. Rieben, High-order curvilinear finite element methods for Lagrangian hydrodynamics, *SIAM Journal on Scientific Computing* 34 (5) (2012) 606–641. 2
- [7] W. Boscheri, M. Dumbser, High order accurate direct Arbitrary-Lagrangian-Eulerian

- ADER-WENO finite volume schemes on moving curvilinear unstructured meshes, *Computers & Fluids* 136 (2016) 48–66. 2
- [8] A. A. Requicha, H. B. Voelcker, Constructive solid geometry, *Production Automation Project*, University of Rochester (25) (1977). 2
- [9] M. Sussman, P. Smereka, S. Osher, A level set approach for computing solutions to incompressible two-phase flow, *Journal of Computational Physics* 114 (1) (1994) 146–159. doi:10.1006/jcph.1994.1155. 2
- [10] J. Sokolowski, J.-P. Zolésio, Introduction to shape optimization, in: *Introduction to shape optimization*, Springer, 1992, pp. 5–12. 2
- [11] G. Allaire, C. Dapogny, P. Frey, Shape optimization with a level set based mesh evolution method, *Computer Methods in Applied Mechanics and Engineering* 282 (2014) 22–53. 2
- [12] M. Hojjat, E. Stavropoulou, K.-U. Bletzinger, The vertex morphing method for node-based shape optimization, *Computer Methods in Applied Mechanics and Engineering* 268 (2014) 494–513. 2
- [13] Z. Q. Xie, R. Sevilla, O. Hassan, K. Morgan, The generation of arbitrary order curved meshes for 3D finite element analysis, *Computational Mechanics* 51 (3) (2013) 361–374. 2
- [14] M. Fortunato, P.-O. Persson, High-order unstructured curved mesh generation using the Winslow equations, *Journal of Computational Physics* 307 (2016) 1–14. 2
- [15] D. Moxey, M. Green, S. Sherwin, J. Peiró, An isoparametric approach to high-order curvilinear boundary-layer meshing, *Computer Methods in Applied Mechanics and Engineering* 283 (2015) 636–650. 2
- [16] A. Gargallo-Peiró, X. Roca, J. Peraire, J. Sarrate, A distortion measure to validate and generate curved high-order meshes on CAD surfaces with independence of parameterization, *International Journal for Numerical Methods in Engineering* 106 (13) (2016) 1100–1130. 2

- [17] T. Toulorge, J. Lambrechts, J.-F. Remacle, Optimizing the geometrical accuracy of curvilinear meshes, *Journal of Computational Physics* 310 (2016) 361–380. 2
- [18] R. Poya, R. Sevilla, A. J. Gil, A unified approach for a posteriori high-order curved mesh generation using solid mechanics, *Computational Mechanics* 58 (3) (2016) 457–490. 2
- [19] E. Ruiz-Gironés, X. Roca, Automatic penalty and degree continuation for parallel preconditioned mesh curving on virtual geometry, *Computer-Aided Design* 146 (2022) 103208. 2
- [20] R. Rangarajan, H. Kabaria, A. Lew, An algorithm for triangulating smooth three-dimensional domains immersed in universal meshes, *International Journal for Numerical Methods in Engineering* 117 (1) (2019) 84–117. 2, 3
- [21] K. Mittal, P. Fischer, Mesh smoothing for the spectral element method, *Journal of Scientific Computing* 78 (2) (2019) 1152–1173. 2
- [22] D. Bommès, B. Lévy, N. Pietroni, E. Puppo, C. Silva, M. Tarini, D. Zorin, Quad-mesh generation and processing: A survey, in: *Computer Graphics Forum*, Vol. 32, Wiley Online Library, 2013, pp. 51–76. 2
- [23] T. J. Baker, Mesh generation: Art or science?, *Progress in Aerospace Sciences* 41 (1) (2005) 29–63. 2
- [24] D. S. Lo, *Finite element mesh generation*, CRC Press, 2014. 2
- [25] L. Chen, H. Wei, M. Wen, An interface-fitted mesh generator and virtual element methods for elliptic interface problems, *Journal of Computational Physics* 334 (2017) 327–348. 3
- [26] Isovalue discretization algorithm.
URL <https://www.mmgtools.org/mmg-remesher-try-mmg/mmg-remesher-options/isovalue-discretization-algorithm> 3

- [27] Y. Ohtake, A. G. Belyaev, Dual-primal mesh optimization for polygonized implicit surfaces with sharp features, *Journal of Computing and Information Science in Engineering* 2 (4) (2002) 277–284. 3, 24
- [28] N. Le Goff, F. Ledoux, S. Owen, Volume preservation improvement for interface reconstruction hexahedral methods, *Procedia Engineering* 203 (2017) 258–270. 3
- [29] P.-O. Persson, G. Strang, A simple mesh generator in MATLAB, *SIAM review* 46 (2) (2004) 329–345. 3
- [30] A. Abdelkader, C. L. Bajaj, M. S. Ebeida, A. H. Mahmoud, S. A. Mitchell, J. D. Owens, A. A. Rushdi, Vorocrust: Voronoi meshing without clipping, *ACM Transactions on Graphics (TOG)* 39 (3) (2020) 1–16. 3
- [31] V. A. Dobrev, P. Knupp, T. V. Kolev, K. Mittal, V. Z. Tomov, The Target-Matrix Optimization Paradigm for high-order meshes, *SIAM Journal of Scientific Computing* 41 (1) (2019) B50–B68. 3, 5
- [32] P. Knupp, Introducing the target-matrix paradigm for mesh optimization by node movement, *Engineering with Computers* 28 (4) (2012) 419–429. 3
- [33] P. Knupp, Target formulation and construction in mesh quality improvement, Tech. Rep. LLNL-TR-795097, Lawrence Livermore National Lab.(LLNL), Livermore, CA (2019). 5, 17
- [34] V. A. Dobrev, P. Knupp, T. V. Kolev, K. Mittal, R. N. Rieben, V. Z. Tomov, Simulation-driven optimization of high-order meshes in ALE hydrodynamics, *Computers & Fluids* (2020). 5
- [35] V. A. Dobrev, P. Knupp, T. V. Kolev, K. Mittal, V. Z. Tomov, HR-adaptivity for nonconforming high-order meshes with the Target-Matrix Optimization Paradigm, *Engineering with Computers* (2021). doi:10.1007/s00366-021-01407-6. 5
- [36] P. Knupp, Metric type in the target-matrix mesh optimization paradigm, Tech. Rep. LLNL-TR-817490, Lawrence Livermore National Lab.(LLNL), Livermore, CA (United States) (2020). 5, 6

- [37] P. Knupp, Geometric parameters in the target matrix mesh optimization paradigm, *Partial Differential Equations in Applied Mathematics* (2022) 100390. 5
- [38] E. Ruiz-Gironés, X. Roca, Automatic penalty and degree continuation for parallel preconditioned mesh curving on virtual geometry, *Computer-Aided Design* 146 (2022) 103208. doi:10.1016/j.cad.2022.103208. 7
- [39] J. Cervený, V. Dobrev, T. Kolev, Nonconforming mesh refinement for high-order finite elements, *SIAM Journal on Scientific Computing* 41 (4) (2019) C367–C392. 10
- [40] P. Fischer, GSLIB: sparse communication library [Software], <https://github.com/gslib/gslib> (2017). 10
- [41] K. Mittal, S. Dutta, P. Fischer, Nonconforming Schwarz-spectral element methods for incompressible flow, *Computers & Fluids* 191 (2019) 104237. 10
- [42] A. G. Belyaev, P.-A. Fayolle, On variational and PDE-based distance function approximations, in: *Computer Graphics Forum*, Vol. 34, Wiley Online Library, 2015, pp. 104–118. 10, 11, 20, 22
- [43] J.-S. Camier, V. Dobrev, P. Knupp, T. Kolev, K. Mittal, R. Rieben, V. Tomov, Accelerating high-order mesh optimization using finite element partial assembly on GPUs, *arXiv preprint arXiv:2205.12721* (2022). 16, 24
- [44] V. A. Garanzha, Polyconvex potentials, invertible deformations, and thermodynamically consistent formulation of the nonlinear elasticity equations, *Computational Mathematics and Mathematical Physics* 50 (9) (2010) 1561–1587. 17
- [45] V. Garanzha, L. Kudryavtseva, S. Utyuzhnikov, Variational method for untangling and optimization of spatial meshes, *Journal of Computational and Applied Mathematics* 269 (2014) 24–41. 17
- [46] T. D. Blacker, S. J. Owen, M. L. Staten, W. R. Quadros, B. Hanks, B. W. Clark, R. J. Meyers, C. Ernst, K. Merkley, R. Morris, et al., Cubit geometry and mesh generation toolkit 15.1 user documentation, Tech. rep., Sandia National Lab.(SNL-NM), Albuquerque, NM (United States) (2016). 22

- [47] M. J. Zahr, A. Shi, P.-O. Persson, Implicit shock tracking using an optimization-based high-order discontinuous Galerkin method, *Journal of Computational Physics* 410 (2020) 109385. 24